Journal of Materials Chemistry C

ROYAL SOCIETY OF CHEMISTRY

PAPER

View Article Online
View Journal

Cite this: DOI: 10.1039/d5tc02966j

Dry ice carbonation approach for the synthesis of calcium carbonate-based magnetic composites

Munirah Ghariani,† Caroline O'Sullivan,† Aran Rafferty and Yurii K. Gun'ko *

Multifunctional magnetic composites that integrate biocompatibility, structural tunability and magnetic responsiveness are highly sought after for advanced biomedical applications. Here, we introduce a previously unexplored dry ice-driven carbonation strategy for the synthesis of $CaCO_3$-coated magnetite (Fe_3O_4@PSS@$CaCO_3$) microstructures, which can be carried out under both aqueous and completely solvent-free, low-temperature conditions. Unlike conventional $CaCO_3$ mineralisation approaches that rely on dissolved carbonate salts and elevated temperatures, this method uniquely employs solid CO_2 (dry ice) as a dual-function reagent, serving simultaneously as a controlled carbonate source and an intrinsic cooling medium. This enables a mild and environmentally benign route to complex magnetic $CaCO_3$ architectures. Strikingly, the choice of reaction medium governs both polymorphism and morphology: aqueous carbonation yields phase-pure rhombohedral calcite microcrystals (≈0.7 μm), whereas the solvent-free dry ice approach produces previously inaccessible acicular microstructures (≈1 μm) comprising a rare coexistence of all three anhydrous $CaCO_3$ polymorphs (calcite, vaterite, and aragonite) under ambient pressure. Structural, compositional, and morphological features were studied using XRD, SEM, FT-IR, and EDX, while SQUID magnetometry confirmed that all composites retain superparamagnetic behaviour, enabling efficient magnetic manipulation despite $CaCO_3$ encapsulation. As a proof of concept, the composites were evaluated as magnetically recoverable drug carriers, using methylene blue as a model compound and doxorubicin as a clinically relevant anticancer drug. UV-Vis spectroscopy revealed efficient drug loading and sustained release, governed by the porosity and polymorphic nature of the $CaCO_3$ shell. By combining the superparamagnetism of Fe_3O_4, the biocompatibility and pH-responsiveness of $CaCO_3$ and a fundamentally new solid-state carbonation paradigm, this work establishes a versatile and sustainable platform for next-generation magnetic materials with strong potential in targeted drug delivery, bioimaging and other magnetically assisted biomedical applications.

Received 5th August 2025,
Accepted 24th February 2026

DOI: 10.1039/d5tc02966j

rsc.li/materials-c

1. Introduction

In recent years, the development of multimodal materials has become a key focus in advanced materials science. The amalgamation of functionalities such as magnetism and biocompatibility into single systems has led to the development of advanced materials with enhanced capabilities in biomedical applications, including magnetic resonance imaging (MRI) contrast enhancement, hyperthermia treatment and biosensing.[1–3] One potential application of these materials is as drug carriers for targeted drug delivery.[4] Conventional methods of drug delivery can face challenges such as poor biodistribution, systemic toxicity and limited targeting efficiency.[5–7] However, these limitations can be mitigated through the use of magnetic nanoparticle (MNP)-based drug delivery systems. These systems can be used for cell-specific targeting, whereby therapeutic agents are entrapped within materials and magnetically guided to a target site (*e.g.* a tumour) using an external magnetic field.[8] This targeted approach can significantly enhance the therapeutic index of drugs by increasing drug concentration at required sites while minimising delivery to off-target tissues.[9] This increased specificity optimises drug bioavailability, reduces side effects faced through systemic administration and improves patient compliance.[10,11]

Magnetic nanoparticles (MNPs) have been widely used in biomedical applications, including targeted drug delivery.[12] This is due to their unique size-dependent physicochemical properties, which differ significantly from those of their bulk counterparts.[13] Their exceptionally high specific surface area, tunable magnetic behaviour and ease of surface functionalisation make them highly versatile for use in biomedicine.[13–16] Among MNPs, magnetite (Fe_3O_4) nanoparticles are of particular

School of Chemistry, CRANN and AMBER Research Centres, Trinity College Dublin, College Green, Dublin 2, Ireland. E-mail: igounko@tcd.ie
† M. G. and C. O'S. contributed equally to this work.

interest for use in biomedicine due to their high biocompatibility, low toxicity and tunable magnetic properties.[17–19] Their size plays a critical role in functionality, with particles smaller than ≈20 nm exhibiting superparamagnetism.[20] This unique magnetic behaviour is highly advantageous in biomedical applications as it prevents unwanted aggregation of MNPs *in vivo* due to remanent magnetisation once an external magnetic field is removed, which can otherwise cause blood vessel blockages (embolism).[21]

Advances in Fe_3O_4 MNP synthesis and surface functionalisation with materials such as drug molecules, fluorescent entities and biominerals has been found to further improve their stability, biocompatibility and specificity for biomedical targets.[2,6,22]

$CaCO_3$ is one of the most abundant minerals found in nature, naturally occurring in limestone, marble, chalk, various marine sediments and plays a crucial role in numerous biological and environmental processes.[23,24] It has attracted significant attention in biomedical applications due to its distinctive properties, including but not limited to, biocompatibility, non-toxicity, and biodegradability.[25–27] $CaCO_3$ nano- and micro-structures have proven to be effective drug carriers in various therapeutic and theranostic applications due to their high loading capacity and porosity.[28,29]

$CaCO_3$ is a polymorphic material and, therefore, its atomic arrangement varies under different external conditions.[30] It exists in three anhydrous polymorphs which are, in order of decreasing thermodynamic stability; rhombohedral calcite, orthorhombic aragonite and hexagonal vaterite.[31,32] While calcite is the most thermodynamically stable form, aragonite and vaterite are metastable conformations at room temperature and atmospheric pressure that can transition into calcite over time or under specific environmental conditions.[28,33] As well as having different crystal structures, the three crystalline phases portray distinctive morphological features which influence key properties such as surface area, porosity and solubility.[31,34] These variations are particularly important in biomedical applications, as porosity plays a crucial role in drug loading and controlled release.[27] Furthermore, porous architectures such as $CaCO_3$-based ones can be loaded with fluorescent moieties for bioimaging applications, allowing real-time tracking of drug distribution *in vivo*.[35–38] Beyond drug delivery, multimodal composites have demonstrated utility in enantiomeric separation, enabling the preferential absorption and isolation of specific enantiomers for pharmaceutical applications.[39,40]

Various magnetic $CaCO_3$ composites have been previously prepared using different co-precipitation synthetic techniques.[41–48]

These reports clearly demonstrated that magnetitic nanoparticles can be successfully occluded or co-precipitated within $CaCO_3$ micro- crystalline matrices, imparting superparamagnetic behavior while preserving crystal calcium carbonate morphologies. The resulting magnetically responsive $CaCO_3$ based structures can be easily manipulated by external magnetic fields and represent a highly adaptable materials platform. By tuning synthesis routes, crystal phase, porosity, and surface functionalization, researchers can tailor magnetic $CaCO_3$ systems for a broad range of applications spanning biomedicine, sensing, catalysis, and environmental remediation, while maintaining scalability, low toxicity, and multifunctionality.

Here, we report a fundamentally new solid-state dry-ice carbonation strategy for the synthesis of Fe_3O_4@PSS@$CaCO_3$ hierarchical microstructures, which can be carried out under completely solvent-free conditions. In contrast to above mentioned conventional synthetic routes that rely on dissolved carbonate salts, elevated temperatures, or complex multistep protocols, this approach introduces dry ice (solid CO_2) as a dual-function reagent, acting simultaneously as a controlled carbonate (CO_3^{2-}) source and as an intrinsic cooling medium (Scheme 1). This unique combination enables low-temperature and environmentally benign synthesis, while offering unique compositions and structural morphologies. This represents a conceptual departure from classical co-precipitation and biomineralization approaches and establishes a new generalizable platform for the sustainable fabrication of $CaCO_3$-based multifunctional materials. The structural, phase and morphological characteristics of the resulting composites were investigated using X-ray diffraction (XRD), scanning electron microscopy (SEM), Fourier-transform infrared spectroscopy (FT-IR) and energy-dispersive X-ray spectroscopy (EDX). Their magnetic response was examined using SQUID vibrating sample magnetometry (VSM), confirming the preservation of superparamagnetic behaviour following $CaCO_3$ encapsulation.

As a proof of concept, we demonstrate the functional utility of these materials in drug delivery applications, employing methylene blue (MB) as a model therapeutic due to its water solubility and strong optical signature. In addition, doxorubicin (DOX) was investigated to highlight the relevance of this platform for clinically important anticancer agents. Drug uptake and release profiles were monitored by UV-Vis spectroscopy, revealing efficient loading and controlled release governed by the $CaCO_3$ matrix. By integrating the superparamagnetic functionality of Fe_3O_4 nanoparticles with the high biocompatibility, pH-responsiveness, and drug-loading capacity of $CaCO_3$, this work

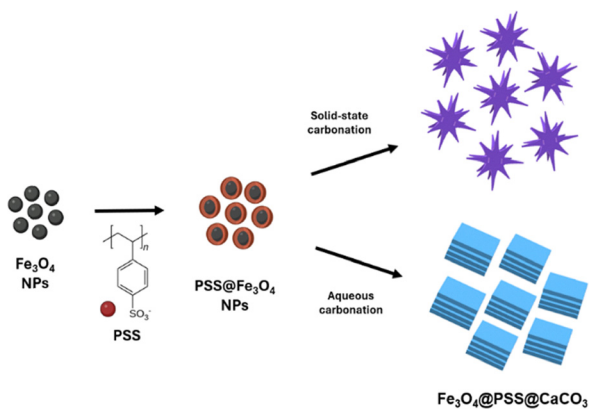

Scheme 1 Schematic illustration of the dry ice carbonation synthetic techniques for the synthesis of Fe_3O_4@PSS@$CaCO_3$ microstructure composites.

delivers a previously unexplored synthetic paradigm for multifunctional hybrid materials.

2. Results and discussion

Initially, Fe_3O_4 magnetic nanoparticles (MNPs) were synthesized using a modified version of a previously reported coprecipitation of Fe^{2+} and Fe^{3+} salt precursors in alkaline conditions under an inert atmosphere in the presence of poly(sodium 4-styrenesulfonate) (PSS).[49] The XRD pattern (Fig. 1a) for the synthesized Fe_3O_4@PSS MNPs displays characteristic Fe_3O_4 diffraction peaks at 2θ values: 18.49, 30.39, 35.72, 37.33, 43.39, 53.70, 57.33, 62.94, which can be assigned to (111), (220), (311), (222), (400), (422), (511) and (440) planes, respectively. Therefore, the magnetite (Fe_3O_4) phase was successfully synthesised. Rietveld refinement of the powder XRD pattern of the Fe_3O_4@PSS particles (Fig. S7) confirms that the sample crystallises in the cubic spinel structure of magnetite (space group $Fd\bar{3}m$), with no additional crystalline impurity phases detected and a refined lattice constant of a = 8.391220 Å. Additionally, crystallite size of the sample was determined by use of the Debye–Scherrer equation, giving an average crystallite size of 11.94 nm.

TEM analysis was carried out on the particles to analyse their size distribution, shape and dispersion. As agglomeration can have a significant impact on the activity of nanoparticles, it is essential to ensure the particles are well dispersed. PSS was incorporated during synthesis to provide electrostatic stabilisation and improve colloidal stability of magnetic nanoparticles. TEM images of the synthesized Fe_3O_4@PSS (Fig. 1c and d) show that the particles were monodispersed with minimal aggregation. This is expected to improve their stability in aqueous media. The particles were quasi-spherical, with a tight, unimodal size distribution and an average diameter of ≈10 nm (Fig. S1), relatively consistent with the crystallite size determined from the XRD pattern of the particles. The interplanar spacing was observed to be approximately 0.25 nm, consistent with the (311) crystallographic plane of cubic Fe_3O_4.[50] The magnetic properties of the Fe_3O_4 MNPs were analysed using magnetometry at 300 K. As shown in the magnetization curves of Fe_3O_4 and Fe_3O_4@PSS (Fig. 1b), bare magnetite and PSS-functionalised magnetite exhibited high saturation magnetization (M_S) values of 91.8 emu g^{-1} and 74.3 emu g^{-1}, respectively. The decrease of saturation magnetization of Fe_3O_4@PSS can be attributed to the non-magnetic nature of PSS. The magnetization curves confirm that the nanoparticles are superparamagnetic in nature, as evidenced by the lack of hysteresis, zero coercivity and absence of remanence. Furthermore, there is no significant change in coercivity upon functionalisation with PSS. To investigate the formation of the polyelectrolyte layer on the Fe_3O_4, zeta (ζ) potential experiments were carried out (Fig. 1e and f).

The graph shows a single peak for both the bare and PSS Fe_3O_4. The adsorption of a single layer of PSS on Fe_3O_4 reversed the zeta potential from +6.87 to −14.6 mV. This decrease in value also signifies enhanced colloidal stability upon addition of the polyelectrolyte layer.[51]

The synthesized Fe_3O_4@PSS MNPs were subsequently combined with $CaCO_3$. For the first time, a "solid-state" dry ice carbonation technique has been employed in the synthesis of $CaCO_3$-based materials. Specifically, the Fe_3O_4@PSS@$CaCO_3$ composites were synthesized in solvent-free conditions, where Fe_3O_4@PSS MNPs were ground together with calcium oxide (CaO) and placed between two layers of dry ice (CO_2) in a freezer at −19 °C. The diffusion of the dry ice through the CaO–Fe_3O_4@PSS material, resulted in the formation of $CaCO_3$-coated Fe_3O_4@PSS particles. This caused unique synergistic effects between both materials, combining their dual functionalities into a single entity.

XRD analysis was used, in the first instance, to determine the dominant polymorphs present in the sample (Fig. 2a). This confirmed the presence of Fe_3O_4 and, interestingly, also confirmed the presence of all three anhydrous polymorphs of $CaCO_3$ (calcite, vaterite and aragonite). Calcite is to be expected, predominantly, as it is the most thermodynamically stable phase of $CaCO_3$. However, a minor proportion of metastable vaterite is also present and, surprisingly, aragonite is also found, even though it typically only forms in extreme conditions of high temperature or pressure.[52,53]

Rietveld refinement of the XRD pattern for the structures synthesized in aqueous conditions (Fig. S8) confirmed the presence of two key phases; magnetite (Fe_3O_4) and calcite ($CaCO_3$). The refinement showed that the sample consisted of

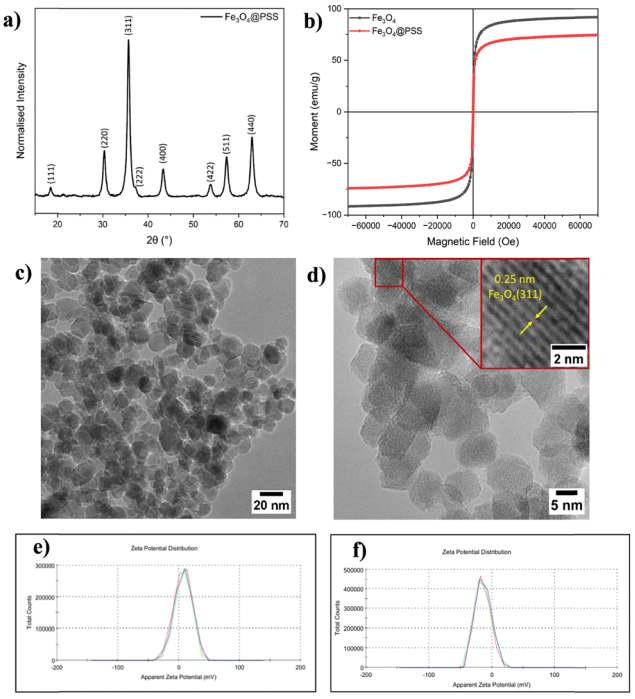

Fig. 1 (a) XRD pattern of Fe_3O_4@PSS MNPs, (b) SQUID VSM curves (taken at 300 K) of Fe_3O_4 and Fe_3O_4@PSS MNPs, (c) and (d) TEM images of Fe_3O_4@PSS MNPs, inset of (d) TEM image displaying interplanar spacing of Fe_3O_4@PSS MNPs, zeta potential (ζ) of (e) Fe_3O_4 MNPs and (f) Fe_3O_4@PSS MNPs.

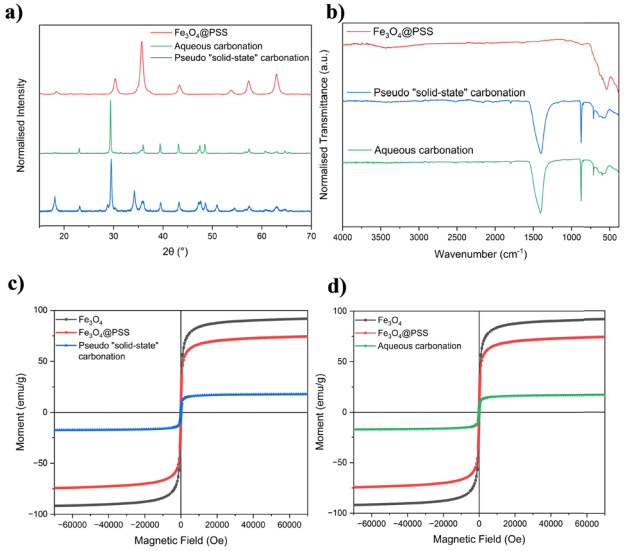

Fig. 2 (a) XRD patterns and (b) FT-IR spectra of Fe_3O_4@PSS and Fe_3O_4@PSS@$CaCO_3$ synthesised *via* aqueous and "solid state" carbonation, SQUID VSM magnetisation curve (taken at 300 K) of Fe_3O_4@PSS@$CaCO_3$ synthesised *via* (c) "solid-state" dry ice carbonation and (d) aqueous dry ice carbonation.

91.68 ± 0.68 wt% calcite and 8.32 ± 0.14 wt% magnetite. Using the (104) peak of the calcite phase, the crystallite size was determined to be 47.86 nm using the Debye–Scherrer equation. The calcite in the sample crystallised in the trigonal structure (space group $R\bar{3}c$) with lattice parameters a, b = 4.99045 Å and c = 17.08263 Å, while the magnetite remained in the cubic inverse spinel structure with a refined lattice parameter of a = 8.38196 Å. The slight decrease in the lattice parameter of magnetite is likely attributed to partial oxidation of Fe^{2+} to Fe^{3+}.

Rietveld refinement of the XRD pattern for the structures produced using the solid-state approach (Fig. S9) confirmed the presence of the three crystalline polymorphic phases of $CaCO_3$; calcite, vaterite and aragonite. Quantitative phase analysis indicates that the solid-state carbonated sample consists predominantly of calcite (57.25 ± 0.63 wt%) with lattice parameters a, b = 4.99045 Å and c = 17.08263 Å. Magnetite accounts for 8.58 ± 0.05 wt% of the crystalline content and retained its cubic inverse spinel structure ($Fd\bar{3}m$), with a refined lattice parameter of a = 8.38196 Å, slightly contracted relative to bulk magnetite. Vaterite ($P6_3/mmc$, a, b = 4.13214 Å, c = 8.49162 Å) and aragonite ($Pnma$, a = 4.96482 Å, b = 7.97194 Å, c = 5.74482 Å) were present as minor phases, accounting for 4.58 ± 0.21 wt% and 2.69 ± 0.14 wt% of the content of the sample, respectively. In addition to these phases, portlandite ($Ca(OH)_2$) was present as a secondary phase (26.90 ± 0.19 wt%), refining in the orthorhombic structure. The presence of this phase indicates successful conversion of the CaO to $Ca(OH)_2$, however it also indicates incomplete conversion of $Ca(OH)_2$ to $CaCO_3$ under solvent-free conditions.

The coexistence of the different solid phases of $CaCO_3$ in the sample suggests that multiple processes including nucleation and growth occur simultaneously. A plausible theory for the stabilization of these metastable phases of $CaCO_3$ is that the dry ice acts as a barrier to crystallization of pure calcite. As the dry ice sublimates and diffuses across the CaO–Fe_3O_4@PSS layer, it generates a supersaturated local CO_2 environment around the material, leading to a gradual release of CO_2 into the system. This controlled release slows down reaction kinetics, thereby reducing the rate at which $CaCO_3$ nucleates and crystallises. In typical aqueous coprecipitation reactions to form $CaCO_3$, rapid crystallization favours the formation of thermodynamically stable calcite. However, in a dry ice-mediated, solvent-free synthesis, the low temperature, as well as slower nucleation and growth kinetics can inhibit transformation of metastable vaterite and aragonite phases to calcite.

FT-IR spectroscopy was used to further confirm the formation of the Fe_3O_4@PSS@$CaCO_3$. The FT-IR spectrum of the Fe_3O_4@PSS MNPs (Fig. 2b) displays a band at ≈555 cm^{-1}, which corresponds to the stretching modes of the tetrahedral and octahedral Fe–O sites.[54] The FT-IR spectra of the Fe_3O_4@PSS@$CaCO_3$ composites further confirms the successful conversion of CaO to $CaCO_3$, with characteristic carbonate (CO_3^{2-}) bands observed in both spectra. In particular, the strong asymmetric C–O stretching band (ν_3) observed at ≈1420 cm^{-1}, together with the sharp out-of-plane C–O bending mode (ν_2) at approximately ≈875 cm^{-1} and the in-plane C–O bending mode (ν_4) at ≈713 cm^{-1}, are characteristic of calcite as the dominant $CaCO_3$ polymorph (Fig. 2b).[55,56]

However, the band overlaps and peak broadening hinder reliable deconvolution of individual vibrational modes, and clear identification of individual $CaCO_3$ polymorphs. The Fe–O stretching vibration of magnetite exhibits a shift to ≈561 cm^{-1} in both composites, potentially attributable to stiffening of the Fe–O bond from slight oxidation of Fe^{2+} to Fe^{3+}.

To verify that these multimodal morphologies still exhibit magnetic behaviour, SQUID VSM analysis was carried out. $CaCO_3$ is a non-magnetic entity and hence, the saturation magnetisation of $CaCO_3$-Fe_3O_4@PSS should be lower, relative to Fe_3O_4 alone. Indeed, the saturation magnetisation of the functional composite was measured as 17.21 emu g^{-1}, representing an approximate 4-fold reduction over Fe_3O_4@PSS (Fig. 2). After encapsulation with $CaCO_3$, the saturation magnetisation was still strong enough to separate the materials from an aqueous solution using magnetic separation, which is ideal. Furthermore, the synthesised composite structures display superparamagnetic behavior, as evidenced by a lack of hysteresis. This is crucial for our intended biomedical application, *i.e.* targeted drug delivery. EDX analysis was employed to determine the elemental composition of the microstructures. Calcium, oxygen, carbon and iron were all detected, as anticipated (Fig. S4). Calcium was present in the highest percentage, followed by oxygen, carbon and iron. This was in agreement with the XRD pattern, which showed $CaCO_3$ as the dominant compound.

SEM images (Fig. 3a) of the microstructures revealed unique, needle-like acicular clusters and rhombohedral structures, which are characteristic of aragonite and calcite,

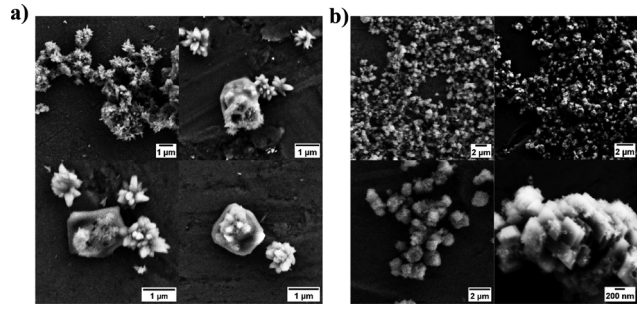

Fig. 3 SEM images of Fe_3O_4@PSS@$CaCO_3$ synthesised using (a) ''solid-state'' dry ice carbonation and (b) aqueous dry ice carbonation synthetic routes.

respectively. The size of the clusters are in the approximate range 0.5–2 μm, with an average size of ≈1 μm (Fig. S2b).

Then the Fe_3O_4@PSS MNPs were also functionalized with $CaCO_3$ using an aqueous dry ice carbonation approach, which our group reported on previously for the synthesis of pure $CaCO_3$ nanoparticles and microspheres.[57] Briefly, a colloidal suspension of Fe_3O_4@PSS MNPs was added to a solution of $Ca(OH)_2$, followed by the sequential addition of dry ice over a period of two hours to form $CaCO_3$-coated Fe_3O_4@PSS particles. XRD analysis was used to determine the phase composition of the sample. The resultant diffraction pattern (Fig. 2a) is in good agreement with the characteristic diffraction peaks of the calcite phase, indicating that phase-pure calcite was produced in the presence of magnetite nanoparticles. SEM images of this sample (Fig. 3b) further confirm the formation of calcite, as is evident from the rhombohedral structures observed. The rhombohedra have an average size of ≈0.7 μm, with sizes ranging from approximately 0.5–1 μm (Fig. S2). As previously stated, calcite is the most thermodynamically stable phase of $CaCO_3$. The structures formed using this synthetic approach were smaller in size, and larger in number, than those produced using the solvent-free approach. This indicates that the crystal nucleation step dominated, at the expense of crystal growth. We further evaluated the magnetic properties of these Fe_3O_4@PSS@$CaCO_3$ composites by magnetometry at 300 K (Fig. 2d). This analysis showed that the composites formed in aqueous conditions had similar magnetic properties to those synthesized in solvent-free conditions, with a saturation magnetization of 17.80 emu g^{-1} observed and the structures exhibiting superparamagnetism. EDX analysis of the samples highlighted that the structures comprised a high percentage of calcium (approximately 25%) (Fig. S5), thus accounting for this decrease in saturation magnetization compared to the Fe_3O_4@PSS MNPs.

Another feature of $CaCO_3$ as a functional material to use for drug delivery systems can be its porous nature. Porosity measurements were conducted on the microstructures using mercury porosimetry and BET surface area analysis techniques. Both methods of synthesis led to markedly different intruded volumes (Fig. 4a and b). Specifically, the aqueous carbonation yielded an intruded volume (3.1 cc g^{-1}) which was approximately three times that of the ''solid state'' (1.0 cc g^{-1}). It's

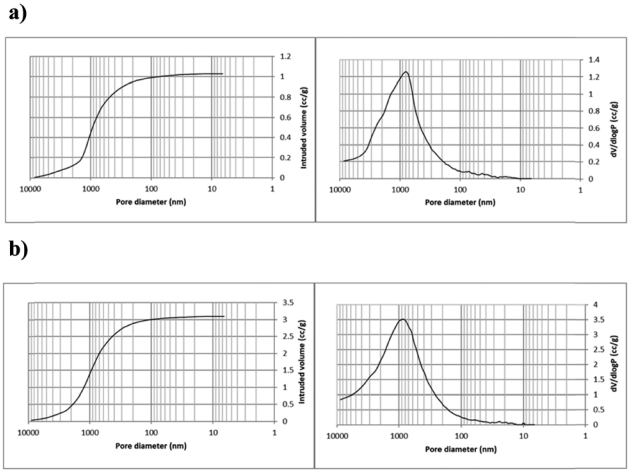

Fig. 4 Mercury intrusion curves and mercury porosimetry pore size distributions of Fe_3O_4@PSS@$CaCO_3$ synthesised *via* (a) ''solid state'' carbonation and (b) aqueous carbonation routes respectively.

important to note that the bulk of this intruded volume is likely due to inter-particulate void space, as opposed to porosity within the particles themselves. When weighing the samples, it was noted that the mass of the aqueous carbonation sample was considerably lower than that of the ''solid-state'' sample, for the same volume of material. In other words, the aqueous carbonation sample has a much lower bulk density, presumably due to having more spaces between the particles, relative to the ''solid state'' sample, due to the way in which the particles pack together. The shapes of the pore size distributions are very similar for the two material types, with a broad peak with maxima *circa*. 800 nm. However, the broadness of the peak means there are pores in a wide range, as large as ≈5 microns and as small as 10 nm. Both samples reveal 'porosity' of note in the range 100–500 nm, and it is believed that some of this is attributable to pores or gaps within the sheet-like rhombohedral structures themselves, as opposed to interparticle voids.

It is worth mentioning that both samples reveal a small but noticeable intrusion of mercury below 50 nm, signifying the presence of mesopores. The microstructures developed using the ''solid-state'' synthesis reveal a relatively low surface area (7 m^2 g^{-1}), relative to the aqueous carbonation method (26 m^2 g^{-1}) as measured using nitrogen gas adsorption (Table S4). On the basis that the mercury porosimetry pore size distributions of the two materials are very similar, the assumption is that it is the particle packing and bulk density characteristics which are the predominant factors governing the surface area value. As was noted above, for a similar mass of sample, the volume, and hence, the surface area of the aqueous carbonation sample will be expected to be higher.

Due to their aforementioned magnetic properties, the composites can be efficiently extracted from solution using an external magnetic field, allowing for effective recycling. This procedure was carried out for the loading and release of the water-soluble model drug using microstructures synthesised using both methods. The entrapment and release of the dye

was investigated to test the materials efficiency as potential drug carriers.

A wide variety of drugs including antibiotics and chemotherapeutics are administered intravenously and hence, the release of the model drug from the pre-loaded microstructures was performed in phosphate buffered saline (PBS) as this solution displays a similar pH to that of blood which is approximately 7.4.[58–60] In our work we initially used the methylene blue (MB) dye as a model for drug uptake and release. The processes have been monitored by UV-vis spectroscopy (Fig. 5). The composites prepared in solution have a greater loading capacity of MB (79.6% loading over 120 hours) than those prepared in solvent-free conditions (42.7% loading over 120 hours) (Fig. 6b).

Additionally, of the initially loaded MB dye into the structures, it was found that 32.4% of this released from those synthesized using an aqueous approach, while 28.2% released from those synthesized using a "solid-state" approach (Fig. 6d).

In addition to using MB as a model drug to investigate the loading and release profiles of the structures, a chemotherapeutic agent, namely doxorubicin (DOX), was also tested. Doxorubicin is a highly potent anticancer agent commonly used in the treatment of various cancers, including breast cancer, ovarian cancer, lymphoma and leukemia.[61,62] Despite its widespread use, its clinical effectiveness is often limited by its rapid systemic clearance, non-specific biodistribution and the development of drug resistance.[63] Furthermore, high DOX concentrations can result in side-effects such as cardiotoxicity, which can lead to irreversible heart damage.[64]

To overcome these limitations, the Fe_3O_4@PSS@$CaCO_3$ structures were explored as controlled and targeted drug delivery systems aimed at enhancing the therapeutic index of DOX. As in the MB studies, the drug loading was performed in phosphate-buffered saline and the loading and release

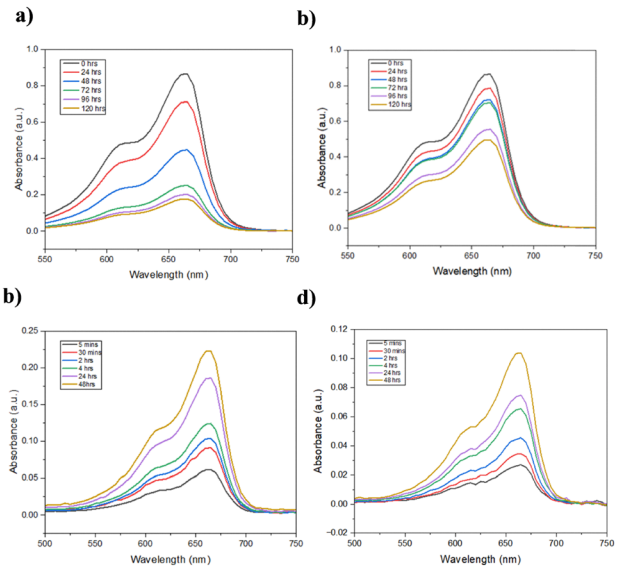

Fig. 5 UV-vis spectra showing loading of MB onto (a) aqueous and (b) "solid state" and the release of methylene blue (MB) from Fe_3O_4@PSS@$CaCO_3$ synthesised using (c) aqueous and (d) "solid state" conditions.

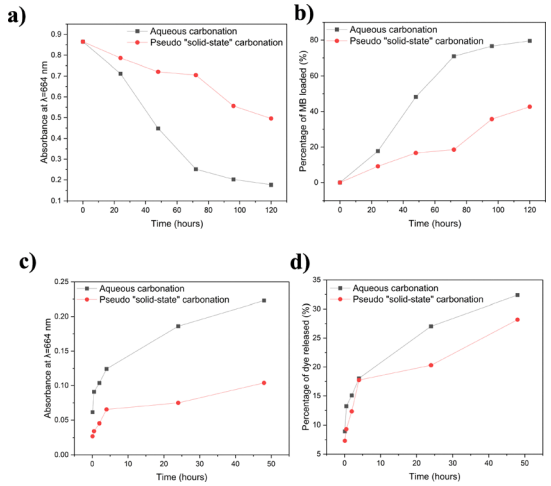

Fig. 6 (a) Absorbance of MB over time for MB loading into structures, (b) percentage of MB (%) adsorbed to Fe_3O_4@PSS@$CaCO_3$ over time, (c) absorbance of MB over time for MB release from structures, (d) percentage of MB (%) desorbed from Fe_3O_4@PSS@$CaCO_3$ over time.

behaviour of the drug was monitored using UV-vis spectroscopy, exploiting the characteristic absorption of the anthracycline chromophore of DOX at 482 nm.[65] A gradual decrease in absorbance at 482 nm was observed for both structures (Fig. 7a and b), indicating progressive DOX uptake by the structures. After 48 hours, the loading efficiency reached 90.4% for the

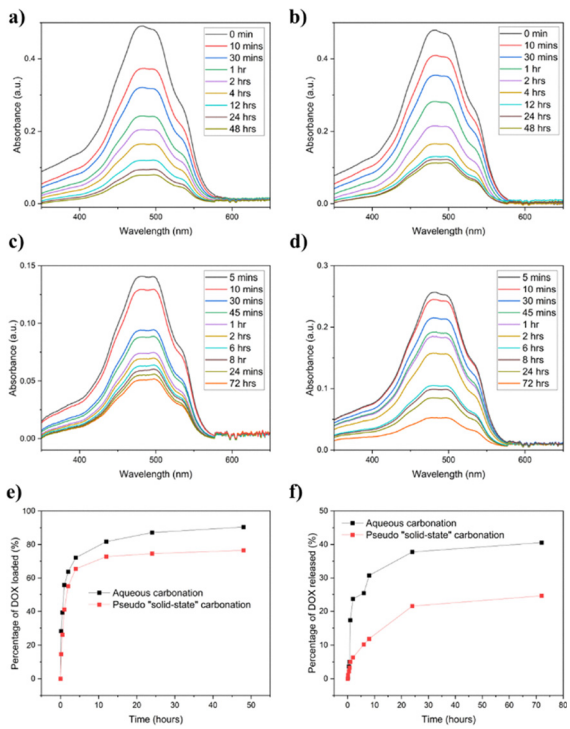

Fig. 7 UV-vis spectra showing loading of DOX onto (a) aqueous and (b) "solid state" structures and the release of DOX from Fe_3O_4@PSS@$CaCO_3$ synthesised using (c) aqueous and (d) "solid state" conditions, (e) percentage of DOX (%) loaded into structures over time and (f) percentage of DOX (%) released from structures over time.

structures synthesised in aqueous conditions and 76.5% for those prepared using the solid-state approach.

Subsequent release studies were conducted by re-dispersing the DOX-loaded structures in PBS. Over a 72-hour period, 40.6% and 24.6% of the initially encapsulated DOX was released from the aqueous and ''solid-state'' structures, respectively. This can be observed from the gradual increase in absorbance at 482 nm (Fig. 7). Both systems exhibited a sustained and controlled release profile, with the structures prepared using the aqueous route displaying a higher cumulative drug release.

The findings from both the study performed with MB and with DOX are in agreement with the porosity measurements performed on the Fe_3O_4@PSS@$CaCO_3$ composites, whereby the microstructures developed using the aqueous approach displayed higher porosity/interparticulate void space. These findings highlight the potential capability of these materials to efficiently load and release drug molecules demonstrating their promise as magnetic drug carriers in targeted drug delivery applications.

3. Experimental

3.1. Materials

All starting materials are commercially available and were used without further purification. The materials used included $FeCl_2 \cdot 4H_2O$ (99%), $FeCl_3 \cdot 6H_2O$ (97%), ammonia solution, (25%, analytical reagent grade), NH_4Cl (99%), poly(sodium 4-styrene sulfonate) ($M_w \approx 70\,000$), Dulbecco's phosphate buffered saline (pH = 7.4), CaO (96%), Methylene blue (>82%), doxorubicin hydrochloride (98%) and ethanol (HPLC grade). Millipore water was obtained using a Synergy 185 Millipore filtration system with a 0.22 μM filter.

3.2. Synthesis of Fe_3O_4 MNPs

Ammonium chloride (NH_4Cl) (0.150 g, 2.80 mmol) was dissolved in degassed Millipore water (150 mL) under N_2 for five minutes. To this, stock (25%) ammonia solution (40 mL, 581 mmol) was added and the reaction was set up for magnetic stirring under N_2 at 80 °C. Separately, $FeCl_2 \cdot 4H_2O$ (0.860 g, 4.32 mmol) and $FeCl_3 \cdot 6H_2O$ (2.33 g, 8.64 mmol) were dissolved in degassed Millipore water (50 mL) under N_2. The iron solution was added dropwise to the ammonia solution, which was then left to stir for two hours under N_2 at 90 °C under reflux. The solution was allowed to cool to room temperature before the product was isolated using magnetic separation. The particles were washed using Millipore water (3 × 20 mL) and ethanol (3 × 20 mL).

3.3. Synthesis of Fe_3O_4@PSS MNPs

Na_2CO_3 (5.290 g, 50 mmol) and poly(sodium 4-styrenesulfonate) (PSS) (0.080 g, 0.43 mmol) were dissolved in degassed Millipore water (200 mL) and heated to 90 °C under N_2. $FeCl_2 \cdot 4H_2O$ (0.248 g, 1.25 mmol) and $FeCl_3 \cdot 6H_2O$ (0.675 g, 2.50 mmol) were dissolved in degassed Millipore water (50 mL) under N_2. This iron solution was added dropwise to the Na_2CO_3-solution. The solution was stirred for two hours at 90 °C under N_2 and under reflux. The particles were washed using Millipore water (3 × 20 mL) and ethanol (3 × 20 mL).

3.4. Aqueous dry ice carbonation synthesis of Fe_3O_4@PSS@$CaCO_3$

PSS-modified Fe_3O_4 (0.015 g) was dispersed in Millipore water (15 mL) and sonicated for 20 minutes. Separately, calcium oxide (CaO) (0.240 g, 4.28 mmol) was added to Millipore water (15 mL) and sonicated for 10 minutes. This solution was added to the Fe_3O_4 solution and this was sonicated for a further 10 minutes. Dry ice pellets (approximately 250 g) were added sequentially over a timescale of two hours.

3.5. ''Solid state'' dry ice carbonation synthesis of Fe_3O_4@PSS@$CaCO_3$

A layer of freshly pressed dry ice (approximately 250 g) was placed in a 500 mL beaker. PSS-modified Fe_3O_4 (0.058 g) and calcium oxide (CaO) (0.060 g, 1.07 mmol) were dispersed evenly on top of the dry ice layer. This was followed by a second layer of dry ice (approximately 250 g) to create a ''sandwich-like'' structure. The beaker was sealed and put in a freezer at −19 °C for 24 hours, after which a further two layers of dry ice (approximately 500 g total) were added. The beaker was once again sealed and put in a freezer at −19 °C for a further 72 hours.

3.6. Loading and release studies of Fe_3O_4@PSS@$CaCO_3$ with methylene blue dye

To load the methylene blue (MB) dye into the structures, Fe_3O_4@PSS@$CaCO_3$ structures (0.015 g) were dispersed in MB (3 mL, 0.025 μM) and left to stand for 24 hours. The particles were then isolated from the methylene blue using magnetic separation with a permanent neodymium magnet. The MB concentration was determined at 664 nm using a UV-vis spectrophotometer at intervals of 24 hours for a total of 120 hours to monitor the loading of the dye into the structures.

The percentage of the MB loaded into the structures was calculated using eqn (1).

$$\text{Percentage of dye loaded (\%)} = \left(\frac{C_0 - C_t}{C_0}\right) \times 100 \qquad (1)$$

where C_0 is the initial MB concentration (mg L^{-1}) and C_t is the MB concentration at different time intervals.

After loading was complete, the structures were magnetically extracted from the dye solution and left to dry in the dark for 96 hours. The particles were dispersed in phosphate-buffered saline solution (pH = 7.4, 3 mL) and the MB concentration was determined at 664 nm using UV-vis spectroscopy at intervals of two hours for a total of 48 hours to monitor the release of the dye from the structures.

The percentage of the MB initially loaded into the structures that was released from the structures was determined using eqn (2).

$$\text{Percentage of dye released (\%)} = \left(\frac{C_t}{C_0}\right) \times 100 \qquad (2)$$

where C_t is the MB concentration at various time intervals (mg L^{-1}) and C_0 is the MB concentration initially loaded.

3.7. Loading and release studies of Fe_3O_4@PSS@$CaCO_3$ with doxorubicin hydrochloride (DOX)

The Fe_3O_4@PSS@$CaCO_3$ structures (20 mg) were dispersed in a solution of doxorubicin hydrochloride (DOX) in phosphate-buffered saline (PBS) (pH = 7.4) (5 mL, 300 μg mL^{-1}) and shaken at 500 RPM on a table mixer. At predetermined time intervals, the particles were isolated from the DOX solution using magnetic separation with a permanent neodymium magnet and a UV-vis spectrum was recorded of the supernatant solution. The microcomposites were then re-dispersed in the DOX solution. The concentration of DOX in the supernatant solution was determined at 482 nm to monitor the loading of the drug into the structures.

$$\text{Percentage of DOX loaded}\,(\%) = \left(\frac{m_0 - m_t}{m_0}\right) \times 100 \qquad (3)$$

where m_0 is the initial mass of DOX added to the loading solution and m_t is the mass of DOX remaining in the supernatant solution at varying times after loading.

To measure the *in vitro* release of the drug, the DOX-loaded structures were magnetically isolated from the DOX solution and left to dry in the dark for 96 hours. The DOX-loaded structures were dispersed in PBS (5 mL). At predetermined intervals, the drug concentration was determined by measuring the absorbance of the supernatant solution at the selected wavelength (λ_{max} = 482 nm) using a UV-vis spectrophotometer. The MCs were then re-dispersed in this solution. The percentage of DOX released from the structures was determined using eqn (4).

$$\text{Percentage of DOX released}\,(\%)(t) = \left(\frac{\sum_{i=1}^{t} m_{\text{released},i}}{m_{\text{loaded}}}\right) \times 100 \qquad (4)$$

where $m_{\text{released},i}$ is the mass of DOX in the supernatant solution at sampling time i, m_{loaded} is the total mass of DOX initially loaded into the structures and t is time (hours).

4. Characterisation techniques

4.1. X-ray diffraction (XRD)

X-ray diffraction was carried out on a Bruker: D2 Phaser 2nd Generation diffractometer using Cu Kα (λ = 1.54184) radiation source from 5 to 70° 2θ with fluorescence, using a zero-background Si sample holder. Rietveld refinement was carried out using the FullProf software (version January-2021). Using the Debye-Sherrer equation (eqn (5)), the mean crystallite size from the most intense diffraction peak of each pattern was calculated.

$$D = \frac{0.9\lambda}{\beta \cos\theta} \qquad (5)$$

where D (nm) is the mean crystallite size, λ (nm) is the wavelength of the X-ray, β (radians) is the full width half maximum (FWHM) and θ (radians) is the Bragg angle.

4.2. Scanning electron microscopy (SEM) and energy dispersive X-ray spectroscopy (EDX)

SEM images were obtained using a Zeiss Ultra Plus Scanning Electron Microscope, with an Oxford Instruments 80 mm^2 XMAX EDX detector used for EDX analysis.

4.3. Transmission electron microscopy (TEM)

TEM images were obtained using a JEOL 2100 instrument operating at 200 kV with a LaB_6 electron source. One drop of sample diluted in ethanol was placed onto a lacey carbon film supported TEM grid and dried.

4.4. Fourier-transform infrared spectroscopy (FT-IR)

FT-IR spectra were obtained using PerkinElmer Spectrum One FT-IR Spectrometer with a diamond UATR. Samples were dried before FT-IR analysis.

4.5. SQUID vibrating sample magnetometry (VSM)

Magnetic measurements were carried out using a Quantum Design Ltd MPMS3 7 Tesla magnetometer (SQUID magnetometer) at 300 K.

4.6. Zeta potential

Zeta potential (ζ) measurements were performed on a Malvern Zeta-Ser Nano series instrument with a laser of 633 nm and scattering angle of 13°. Measurements were taken at 25 °C in Millipore H_2O.

4.7. Ultraviolet-visible spectroscopy (UV-vis)

UV-vis absorption spectra were recorded using a PerkinElmer LAMBDA 1050 UV/vis/NIR spectrophotometer. The particles were dissolved in solution and placed in a quartz cuvette with a path length of 1 cm for measurement.

4.8. Mercury porosimetry and BET

Mercury porosimetry was performed using an Autoscan-33 Porosimeter (Quantachrome, Hampshire, UK). The pore diameter D was calculated according to the Washburn equation (eqn (6)):

$$D = \frac{-4\gamma \cos\theta}{P} \qquad (6)$$

where θ is the contact angle between the solid and mercury, γ is the surface tension of mercury (485 dyne cm^{-1}), and P is the hydraulic pressure applied to force penetration of the mercury into the pores. A default contact angle of 140° was used.

Specific surface area was determined by nitrogen (N_2) adsorption measurements performed at 77 K using a Nova 4200e Surface Area Analyzer (Quantachrome, UK). The specific surface area of the samples was calculated from the N_2 adsorption data at relative pressures between 0.1 and 0.30, by employing the Brunauer–Emmett–Teller (BET) multi-point method. All

samples were outgassed at 150 °C under vacuum for 15 h prior to the analysis.

5. Conclusions

In conclusion, for the first time, we have used a dry ice-mediated solid-state carbonation approach to magnetic $CaCO_3$-based composites. This resulted in the advancements such as in mild, low-temperature synthesis without any solvents, simultaneous stabilisation of all three anhydrous $CaCO_3$ polymorphs under ambient pressure and the formation of unique acicular $CaCO_3$ microstructures not accessible *via* conventional aqueous routes. We have also produced a phase-pure calcite-coated Fe_3O_4@PSS sample by aqueous dry ice carbonation, with no other polymorphs of $CaCO_3$ found. The dry-ice-driven carbonation process allows $CaCO_3$ to be deposited directly onto polymer-stabilized magnetic nanoparticles, yielding well-defined composite architectures without the need for harsh reagents, high pH conditions or excess solvent. All materials produced using this dry ice carbonation technique exhibited superparamagnetic behaviour, with saturation magnetisation values of 17.80 and 17.21 emu g^{-1} for those synthesised using aqueous and solvent-free approaches, respectively. Mercury porosimetry measurements revealed the high porosity/low bulk density of the structures, while loading and release studies of a cationic dye and doxorubicin portrayed the high drug loading capacity of the structures. Overall, these results highlight the Fe_3O_4@PSS@$CaCO_3$ composites as a versatile and promising platform for potential biomedical applications such as drug carrier development, particularly for magnetically assisted and pH-responsive targeted drug delivery applications. Our future work will focus on systematic cytotoxicity assessments and comprehensive *in vitro* cell-based studies to establish biocompatibility and cellular uptake mechanisms. In parallel, we plan to investigate in detail the loading and release of clinically relevant therapeutic agents, and explore various surface functionalisation strategies for active targeting, and assess the influence of $CaCO_3$ polymorphism and porosity on drug delivery performance.

Author contributions

Munirah Ghariani: conceptualisation (equal); data curation (equal); formal analysis (equal); investigating (equal); writing – original draft (equal); writing – review & editing (equal). Caroline O'Sullivan: conceptualisation (equal); data curation (equal); formal analysis (equal); investigating (equal); writing – original draft (equal); writing – review & editing (equal). Aran Rafferty: data curation (supporting); writing – review & editing (supporting). Yurii K. Gun'ko: conceptualisation (lead); supervision (lead); writing – review & editing (supporting).

Conflicts of interest

There are no conflicts to declare.

Data availability

Data are available upon request from the authors.

Supplementary information (SI) includes zeta potential measurements, particle size distributions, electron microscopy images, EDX analysis, BET surface area measurements, and Rietveld refinement data. See DOI: https://doi.org/10.1039/d5tc02966j.

Acknowledgements

We extend thanks to the CTD-ACM, Research Ireland (projects: SFI-20/FFP-A/8904 and 21/RC/10307_P2) and AMBER for their support of this work. This work was supported by Research Ireland 18/EPSRC-CDT-3581 and the Engineering and Physical Sciences Research Council EP/S023259/1. All microscopy characterization and analysis has been performed at the CRANN Advanced Microscopy Laboratory (AML).

References

1 Y. Q. Meng, Y. N. Shi, Y. P. Zhu, Y. Q. Liu, L. W. Gu, D. D. Liu, A. Ma, F. Xia, Q. Y. Guo, C. C. Xu, J. Z. Zhang, C. Qiu and J. G. Wang, *J. Nanobiotechnol.*, 2024, **22**, 1–28.
2 R. S. García, S. Stafford and Y. K. Gun'ko, *Appl. Sci.*, 2018, **8**, 12–16.
3 B. E. Keshta, A. H. Gemeay, D. Kumar Sinha, S. Elsharkawy, F. Hassan, N. Rai and C. Arora, *Results Chem.*, 2024, **7**, 101388.
4 J. Chomoucka, J. Drbohlavova, D. Huska, V. Adam, R. Kizek and J. Hubalek, *Pharmacol. Res.*, 2010, **62**, 144–149.
5 Y. Dang and J. Guan, *Smart Mater. Med.*, 2020, **1**, 10–19.
6 M. Salehirozveh, P. Dehghani and I. Mijakovic, *J. Funct. Biomater.*, 2024, **15**, 1–34.
7 A. Sultana, M. Zare, V. Thomas, T. S. S. Kumar and S. Ramakrishna, *Med. Drug Discovery*, 2022, **15**, 100134.
8 M. J. Mitchell, M. M. Billingsley, R. M. Haley, M. E. Wechsler, N. A. Peppas and R. Langer, *Nat. Rev. Drug Discovery*, 2021, **20**, 101–124.
9 J. F. Liu, B. Jang, D. Issadore and A. Tsourkas, *Wiley Interdiscip. Rev. Nanomed. Nanobiotechnol.*, 2019, **11**, 1–18.
10 Q. A. Pankhurst, N. K. T. Thanh, S. K. Jones and J. Dobson, *J. Phys. D: Appl. Phys.*, 2009, **42**, 224001.
11 M. Zhang, S. Gao, D. Yang, Y. Fang, X. Lin, X. Jin, Y. Liu, X. Liu, K. Su and K. Shi, *Acta Pharm. Sin. B*, 2021, **11**, 2265–2285.
12 E. M. Materón, C. M. Miyazaki, O. Carr, N. Joshi, P. H. S. Picciani, C. J. Dalmaschio, F. Davis and F. M. Shimizu, *Appl. Surf. Sci. Adv.*, 2021, **6**, 100163.
13 A. G. Díez, M. Rincón-Iglesias, S. Lanceros-Méndez, J. Reguera and E. Lizundia, *Mater. Today Chem.*, 2022, **26**, 101220.
14 A. Jordan, R. Scholz, P. Wust, H. Fähling and R. Felix, *J. Magn. Magn. Mater.*, 1999, **201**, 413–419.
15 V. V. Mody, A. Cox, S. Shah, A. Singh, W. Bevins and H. Parihar, *Appl. Nanosci.*, 2014, **4**, 385–392.

16 J. You, L. Wang, Y. Zhao and W. Bao, *J. Cleaner Prod.*, 2021, **281**, 124668.
17 S. Delice, M. Isik and N. M. Gasanly, *Chem. Phys. Lett.*, 2024, **840**, 141139.
18 L. S. Ganapathe, M. A. Mohamed, R. M. Yunus and D. D. Berhanuddin, *Magnetochemistry*, 2020, **6**, 1–35.
19 M. R. Ghazanfari, M. Kashefi, S. F. Shams and M. R. Jaafari, *Biochem. Res. Int.*, 2016, **2016**, 7840161.
20 K. Wu and J. P. Wang, *AIP Adv.*, 2017, 7.
21 K. Vasić, Ž. Knez and M. Leitgeb, *J. Funct. Biomater.*, 2024, **15**, 227.
22 B. W. Chen, Y. C. He, S. Y. Sung, T. T. H. Le, C. L. Hsieh, J. Y. Chen, Z. H. Wei and D. J. Yao, *Sci. Technol. Adv. Mater.*, 2020, **21**, 471–481.
23 J. Chen and L. Xiang, *Powder Technol.*, 2009, **189**, 64–69.
24 M. B. Toffolo, G. Ricci, L. Caneve and I. Kaplan-Ashiri, *Sci. Rep.*, 2019, **9**, 1–15.
25 H. Liu, Z. Wen, Z. Liu, Y. Yang, H. Wang, X. Xia, J. Ye and Y. Liu, *Acta Pharm. Sin. B*, 2024, **14**, 602–622.
26 S. Biradar, P. Ravichandran, R. Gopikrishnan, V. Goornavar, J. C. Hall, V. Ramesh, S. Baluchamy, R. B. Jeffers and G. T. Ramesh, *J. Nanosci. Nanotechnol.*, 2011, **11**, 6868–6874.
27 P. Zhao, Y. Tian, J. You, X. Hu and Y. Liu, *Bioengineering*, 2022, **9**, 691.
28 Y. Wei, R. Sun, H. Su, H. Xu, L. Zhang, D. Huang, Z. Liang, Y. Hu, L. Zhao and X. Lian, *Colloids Surf., B*, 2021, **199**, 111545.
29 C. Lin, M. Akhtar, Y. Li, M. Ji and R. Huang, *Pharmaceutics*, 2024, **16**, 275.
30 M. Ni and B. D. Ratner, *Surf. Interface Anal.*, 2008, **40**, 1356–1361.
31 F. Liendo, M. Arduino, F. A. Deorsola and S. Bensaid, *Powder Technol.*, 2022, **398**, 117050.
32 B. Myszka, M. Schüßler, K. Hurle, B. Demmert, R. Detsch, A. R. Boccaccini and S. E. Wolf, *RSC Adv.*, 2019, **9**, 18232–18244.
33 J. Aufort and R. Demichelis, *Cryst. Growth Des.*, 2020, **20**, 8028–8038.
34 R. Febrida, A. Cahyanto, E. Herda, V. Muthukanan, N. Djustiana, F. Faizal, C. Panatarani and I. M. Joni, *Materials*, 2021, **14**, 4425.
35 S. Guo, M. Yang, M. Chen, J. Zhang, K. Liu, L. Ye and W. Gu, *Dalton Trans.*, 2015, **44**, 8232–8237.
36 M. Fujiwara, K. Shiokawa, T. Kubota and K. Morigaki, *Adv. Powder Technol.*, 2014, **25**, 1147–1154.
37 M. K. Lima-Tenório, E. A. Gómez Pineda, N. M. Ahmad, H. Fessi and A. Elaissari, *Int. J. Pharm.*, 2015, **493**, 313–327.
38 A. S. Drozdov, K. S. Komarova, E. N. Mochalova, E. N. Komedchikova, V. O. Shipunova and M. P. Nikitin, *Int. J. Mol. Sci.*, 2023, **24**, 134.
39 S. Ghosh, T. H. Fang, M. S. Uddin and K. Hidajat, *Colloids Surf., B*, 2013, **105**, 267–277.
40 A. Hu, G. T. Yee and W. Lin, *J. Am. Chem. Soc.*, 2005, **127**, 12486–12487.
41 A. Sergeeva, R. Sergeev, E. Lengert, A. Zakharevich, B. Parakhonskiy, D. Gorin, S. Sergeev and D. Volodkin, *ACS Appl. Mater. Interfaces*, 2015, **7**, 21315–21325.
42 R. F. Fakhrullin, A. G. Bikmullin and D. K. Nurgaliev, *ACS Appl. Mater. Interfaces*, 2009, **1**, 1847–1851.
43 M. Mihai, V. Socoliuc, F. Doroftei, E. L. Ursu, M. Aflori, L. Vekas and B. C. Simonescu, *Cryst. Growth Des.*, 2013, **13**, 3535–3545.
44 L. Zhang, R. Huang, P. Tao, C. Song, J. Wu, T. Deng and W. Shang, *Pure Appl. Chem.*, 2017, **89**, 1741–1750.
45 N. E. Markina, A. V. Markin, A. M. Zakharevich and I. Y. Goryacheva, *Microchim. Acta*, 2017, **184**, 3937–3944.
46 P. Xue, M. Hou, L. Sun, Q. Li, L. Zhang, Z. Xu and Y. Kang, *Acta Biomater.*, 2018, **81**, 242–255.
47 P. Wang, T. Shen, X. Li, Y. Tang and Y. Li, *ACS Appl. Nano Mater.*, 2020, **3**, 1272–1281.
48 W. Liu, S. Yin, Y. Hu, T. Deng and J. Li, *Anal. Chem.*, 2021, **93**, 14223–14230.
49 F. Yazdani and M. Seddigh, *Mater. Chem. Phys.*, 2016, **184**, 318–323.
50 X. Lu, R. Wang, Y. Bai, J. Chen and J. Sun, *J. Mater. Chem. A*, 2015, **3**, 12031–12037.
51 D. J. Pochapski, C. Carvalho Dos Santos, G. W. Leite, S. H. Pulcinelli and C. V. Santilli, *Langmuir*, 2021, **37**, 13379–13389.
52 N. Koga, D. Kasahara and T. Kimura, *Cryst. Growth Des.*, 2013, **13**, 2238–2246.
53 P. Forjanes, J. M. Astilleros and L. Fernández-Díaz, *Earth Planet. Sci. Lett.*, 2024, **639**, 118771.
54 A. Miri, H. Najafzadeh, M. Darroudi, M. J. Miri, M. A. J. Kouhbanani and M. Sarani, *ChemistryOpen*, 2021, **10**, 327–333.
55 J. D. Rodriguez-Blanco, S. Shaw and L. G. Benning, *Nanoscale*, 2011, **3**, 265–271.
56 T. Elgayyar, F. Azzolina-Jury and F. Thibault-Starzyk, *Phys. Chem. Chem. Phys.*, 2025, **27**, 22871–22879.
57 F. C. Donnelly, F. Purcell-Milton, V. Framont, O. Cleary, P. W. Dunne and Y. K. Gun'ko, *Chem. Commun.*, 2017, **53**, 6657–6660.
58 S. Spencer, H. Ipema, P. Hartke, C. Krueger, R. Rodriguez, A. E. Gross and M. Gabay, *Hosp. Pharm.*, 2018, **53**, 157–169.
59 S. Fouliard, M. Chenel and F. Marcucci, *Front. Oncol.*, 2013, **3**, 192.
60 J. A. Kellum, *Crit. Care*, 2000, **4**, 6–14.
61 M. Kciuk, A. Gielecińska, S. Mujwar, D. Kołat, Ż. Kałuzińska-Kołat, I. Celik and R. Kontek, *Cells*, 2023, **12**, 26–32.
62 A. Bisht, D. Avinash, K. K. Sahu, P. Patel, G. D. Gupta and B. D. Kurmi, *Drug Delivery Transl. Res.*, 2025, **15**, 102–133.
63 J. M. Llovet and J. Bruix, *Hepatology*, 2003, **37**, 429–442.
64 P. S. Rawat, A. Jaiswal, A. Khurana, J. S. Bhatti and U. Navik, *Biomed. Pharmacother.*, 2021, **139**, 111708.
65 N. Rahoui, B. Jiang, N. Taloub, M. Hegazy and Y. D. Huang, *J. Biomater. Sci., Polym. Ed.*, 2018, **29**, 1482–1497.

